

## Ammonia-assisted Fast Li-ion Conduction in A New Ammine Lithium Borohydride, $\text{LiBH}_4 \cdot \frac{1}{2}\text{NH}_3$

Yigang Yan, Jakob B. Grinderslev, Young-Su Lee, Mathias Jørgensen, Young  
Whan Cho, Radovan Černý, Torben R. Jensen\*

### Electronic Supplementary Information (ESI)

#### Experimental Methods:

Chemicals of  $\text{LiBH}_4$  ( $\geq 95\%$ ),  $\text{LiNH}_2$  (95%),  $\text{LiOH}$  ( $\geq 98\%$ ) and  $\text{Li}_2\text{O}$  (97%, -60 mesh powder) were purchased from Sigma-Aldrich. Solid-state synthesis of  $\text{LiBH}_4 \cdot \frac{1}{2}\text{NH}_3$  (**s1**) was carried out by mechanical milling of  $\text{LiBH}_4$ ,  $\text{LiNH}_2$  and  $\text{LiOH}$  in a molar ratio of 2:1:1, followed by heat treatment ( $T = 80$  °C for 12 hours under Ar atmosphere).  $\text{Li}(\text{BH}_4)_{0.25}(\text{NH}_2)_{0.75}$  was synthesized by mechanical milling of  $\text{LiBH}_4$  and  $\text{LiNH}_2$  in a molar ratio of 1:3, followed by a heat treatment ( $T = 120$  °C for 12 hours under Ar atmosphere). The ball milling procedures producing sample **s1** and  $\text{Li}(\text{BH}_4)_{0.25}(\text{NH}_2)_{0.75}$  were carried out for 5 min with a 2 min pause for 5 and 59 repetitions, respectively, at a speed of 350 rpm and a ball-to-powder weight ratio of 25:1 using 5 tungsten carbide (WC) balls and a WC vial.

$\text{LiBH}_4 \cdot \text{NH}_3$  was synthesized by exposure of  $\text{LiBH}_4$  to dry ammonia gas at a pressure of 1 bar for 2 h at  $T = -10$  °C, after which it was dried *in vacuo* for 1 hour. Synthesis of sample  $\text{LiBH}_4 \cdot \frac{1}{2}\text{NH}_3$  (**s2**) was performed by mechanical milling of  $\text{LiBH}_4 \cdot \text{NH}_3$  and  $\text{LiBH}_4$  in 1:1 molar ratio. Sample **s3**, was synthesized by ball milling a mixture of **s1** and  $\text{Li}(\text{BH}_4)_{0.25}(\text{NH}_2)_{0.75}$  in mass ratio of 1:3, and sample **s4**, was synthesized by ball milling a mixture of **s1** and  $\text{Li}_2\text{O}$  in mass ratio of 1:4. The mechanical milling procedures producing samples **s2**, **s3** and **s4** were carried out for 2 min with a 2 min pause for 5 repetitions at a speed of 200 rpm and a ball-to-powder weight ratio of 15:1 using 3 tungsten carbide (WC) balls and a WC vial.

Powder X-ray Diffraction (PXRD) data were collected at room temperature on a Rigaku SMARTLAB diffractometer, equipped with a rotating Cu anode (Cu  $K\alpha_1$  radiation, 2 kW,  $\lambda = 1.5406$  Å). The samples were packed in 0.5 mm o.d. capillary tubes in the glove box, sealed with glue, and transferred to the instrument without air exposure. *In situ* synchrotron radiation powder X-ray diffraction (SR-PXD) data of the  $\text{LiBH}_4 \cdot \frac{1}{2}\text{NH}_3$  were collected at the I11 beamline at the Diamond Light Source, England, with  $\lambda = 0.825850$  Å. The sample was heated up using a heat blower with a ramp rate of 5 °C/min.

Electrochemical impedance spectroscopy (EIS) data were collected on a BioLogic MTZ-35 impedance analyzer equipped with a high-temperature sample holder. Samples were pressed into 6.35 mm diameter pellets of ca. 1 mm thickness under the pressure of 0.63 GPa. All measurements were conducted in an argon atmosphere, and the temperature was measured by a K-type thermocouple 5 mm from the sample. Impedance data were measured at 20 mV ac from 3 MHz to 1 Hz. Ion conductivity data ( $\sigma$ ) were derived from Nyquist impedance plots using the x-intercept of the Nyquist semicircle (R), area of the pellet face (A), and pellet thickness (t) according to:  $\sigma = t/(R \times A)$ . Cyclic voltammetry (CV) was measured using a BioLogic VMP3 multi-channel potentiostat.

Thermogravimetric analysis (TGA) and differential scanning calorimetry (DSC) was conducted on a PerkinElmer STA 6000, where 3–5 mg samples were placed in  $\text{Al}_2\text{O}_3$  crucibles and heated at 5 °C per min under constant argon flow ( $50 \text{ mL} \cdot \text{min}^{-1}$ ). Simultaneous mass spectrometry (MS) was collected for  $\text{H}_2$  ( $m/z = 2$ ) and  $\text{NH}_3$  ( $m/z = 17$ ), using a Hiden Analytical HPR-20 QMS sampling system. All sample handling was carried out in an Ar-circulated glove box with  $\text{O}_2 < 0.1$  ppm and  $\text{H}_2\text{O} < 0.1$  ppm.

---

## Computational Methods

The migration path for  $\text{Li}^+$  was calculated from first-principles using the Vienna Ab-initio Simulation Package.<sup>1, 2</sup> The calculations were performed within the framework of density functional theory (DFT) employing the generalized-gradient approximation by Perdew, Burke, and Ernzerhof for exchange-correlation functional.<sup>3</sup> Projector augmented wave potential with a planewave cutoff energy of 600 eV was used.<sup>4</sup>  $\text{Li}^+$  interstitial is often the major charge carrier in this kind of  $\text{LiBH}_4$ -based ionic conductor.<sup>5-7</sup> Therefore, stable  $\text{Li}^+$  interstitial sites were located using the supercell containing 24 formula units of  $\text{LiBH}_4 \cdot \frac{1}{2}\text{NH}_3$  plus one interstitial ion. Then the minimum energy path through some of the most stable sites was obtained by the climbing-image nudged elastic band method<sup>8</sup> with a supercell of doubled unit cells in the  $c$  direction. Only migration along the  $c$  direction was considered as the jump distance between the stable sites along the  $a$  direction is as large as  $\sim 4.8 \text{ \AA}$  (half the lattice parameter  $a$ ), which would not occur frequently, whereas it is only  $\sim 2 \text{ \AA}$  along the  $c$  direction.

The bond-valence-based empirical force field calculations have been performed using the program SoftBV.<sup>9</sup> The ions used for calculations were  $\text{Li}^+$  (mobile ion),  $\text{B}^{3+}$ ,  $\text{N}^{5+}$ ,  $\text{H}^-$ . The minima energy surfaces were drawn using the program Vesta.<sup>10</sup>

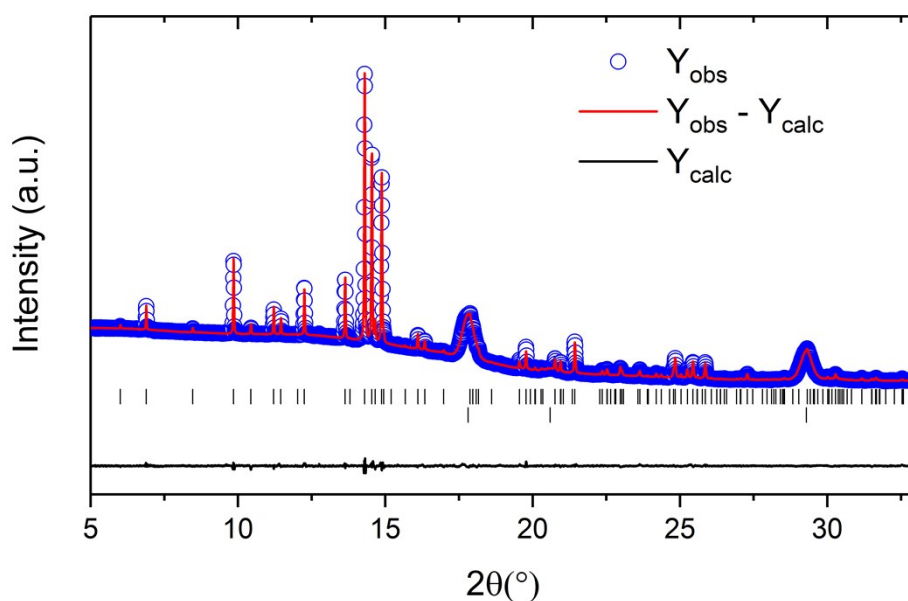


**Figure S1.** Rietveld refinement of PXD data of **s1** measured at room temperature,  $\lambda = 0.825850 \text{ \AA}$ , showing experimental (blue circles) and calculated (red line) PXD patterns, and a difference plot below (black line). Top tick ( $\text{LiBH}_4 \cdot \frac{1}{2}\text{NH}_3$ , 66.9 wt%), bottom tick ( $\text{Li}_2\text{O}$ , 33.1 %). Final discrepancy factors:  $R_p = 0.62 \%$ ,  $R_{wp} = 0.93 \%$  (not corrected for background),  $R_p = 9.22 \%$ ,  $R_{wp} = 5.86 \%$  (conventional Rietveld  $R$ -factors),  $R_{\text{Bragg}}(\text{LiBH}_4 \cdot \frac{1}{2}\text{NH}_3) = 3.41 \%$ ,  $R_{\text{Bragg}}(\text{Li}_2\text{O}) = 0.319 \%$  and global  $\chi^2 = 5.81$ .  $\text{LiBH}_4 \cdot \frac{1}{2}\text{NH}_3$ : space group  $Pna2_1$ ,  $a = 9.6174(7)$ ,  $b = 13.7476(9)$ ,  $c = 4.4409(5) \text{ \AA}$ ;  $\text{Li}_2\text{O}$ : space group  $Fm\text{-}3m$ ,  $a = 4.6195(8) \text{ \AA}$ .

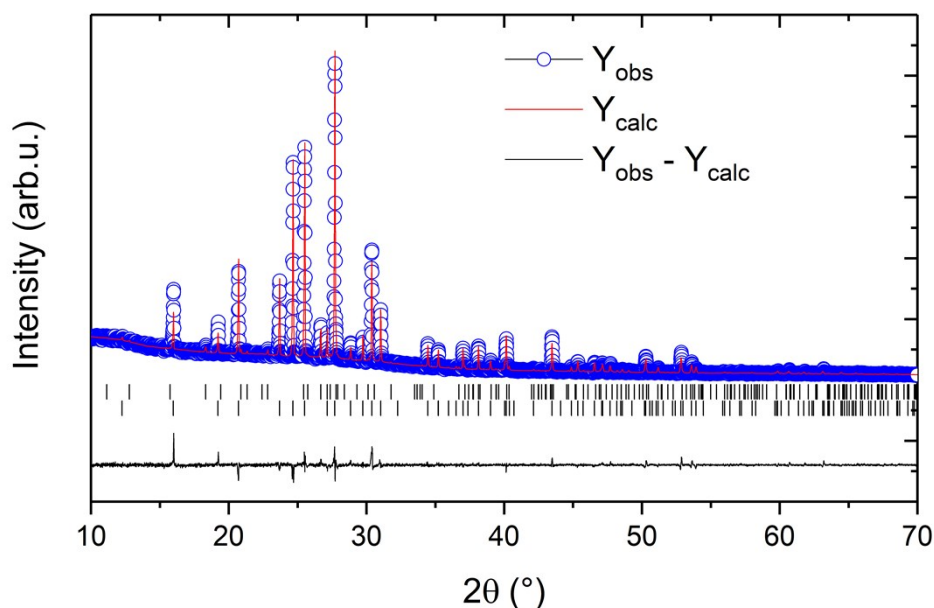


**Figure S2.** Rietveld refinement of PXD data of  $\text{LiBH}_4 \cdot \text{NH}_3$  measured at room temperature,  $\lambda = 1.54056 \text{ \AA}$ , showing experimental (blue circles) and calculated (red line) PXD patterns, and a difference plot below (black line). Top tick ( $\text{LiBH}_4 \cdot \frac{1}{2}\text{NH}_3$ , 6.0 wt%), bottom tick ( $\text{LiBH}_4 \cdot \text{NH}_3$ , 94.0 %). Final discrepancy factors:  $R_p = 4.04 \%$ ,  $R_{wp} = 5.85 \%$  (not corrected for background),  $R_p = 30.6 \%$ ,  $R_{wp} = 20.6 \%$  (conventional Rietveld  $R$ -factors),  $R_{\text{Bragg}}(\text{LiBH}_4 \cdot \frac{1}{2}\text{NH}_3) = 15.8 \%$ ,  $R_{\text{Bragg}}(\text{LiBH}_4 \cdot \text{NH}_3) = 7.70 \%$  and global  $\chi^2 = 10$ .  $\text{LiBH}_4 \cdot \frac{1}{2}\text{NH}_3$ : space group  $Pna2_1$ ,  $a = 9.6178(1)$ ,  $b = 13.7480(2) \text{ \AA}$ ,  $c = 4.44104(5) \text{ \AA}$ ;  $\text{LiBH}_4 \cdot \text{NH}_3$ : space group  $Pnma$ ,  $a = 5.9994(8)$ ,  $b = 4.4854(8)$ ,  $c = 14.4162(4) \text{ \AA}$ .

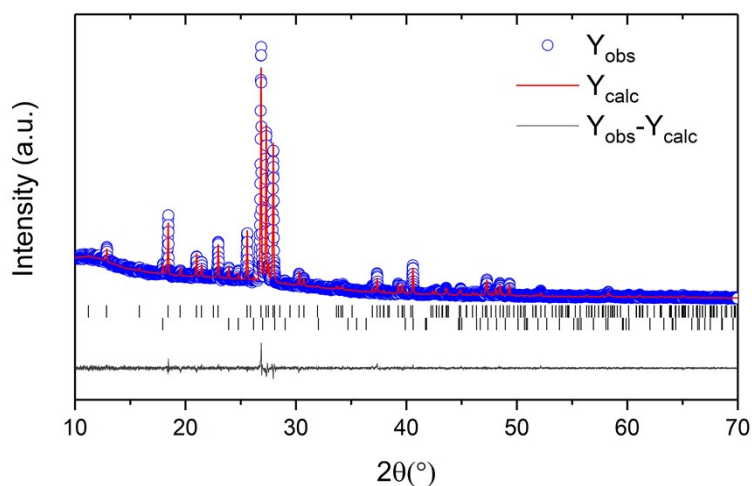


**Figure S3.** Rietveld refinement of PXD data of **s2** measured at room temperature,  $\lambda = 1.54056 \text{ \AA}$ , showing experimental (blue circles) and calculated (red line) PXD patterns, and a difference plot below (black line). Top tick ( $\text{LiBH}_4 \cdot \frac{1}{2}\text{NH}_3$ , 94.8 wt%), bottom tick ( $\text{LiBH}_4$ , 5.2 %). Final discrepancy factors:  $R_p = 3.45 \%$ ,  $R_{wp} = 4.53 \%$  (not corrected for background),  $R_p = 28.3 \%$ ,  $R_{wp} = 17.7 \%$  (conventional Rietveld  $R$ -factors),  $R_{\text{Bragg}}(\text{LiBH}_4 \cdot \frac{1}{2}\text{NH}_3) = 6.01 \%$ ,  $R_{\text{Bragg}}(\text{LiBH}_4) = 12.6 \%$  and global  $\chi^2 = 1.15$ .  $\text{LiBH}_4 \cdot \frac{1}{2}\text{NH}_3$ : space group  $Pna2_1$ ,  $a = 9.6178(1)$ ,  $b = 13.7480(2) \text{ \AA}$ ,  $c = 4.44104(5) \text{ \AA}$ ;  $\text{LiBH}_4$ : space group  $Pnma$ ,  $a = 7.141$ ,  $b = 4.431$ ,  $c = 6.748 \text{ \AA}$ .

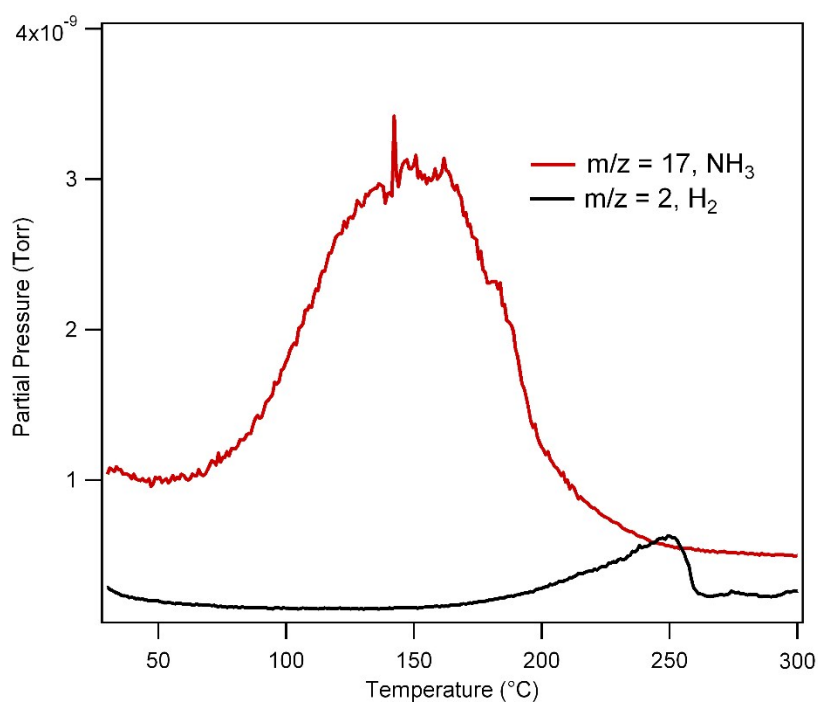


**Figure S4.** MS profiles of sample **s1**.

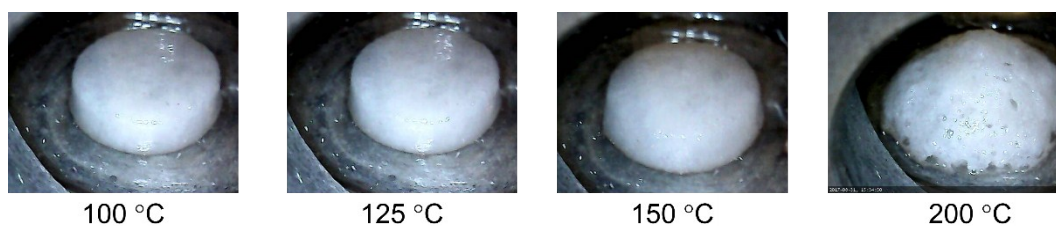


**Figure S5.** Image of the **s1** pellet heated to 200 °C in argon atmosphere with a heating rate of 5 °C/min.

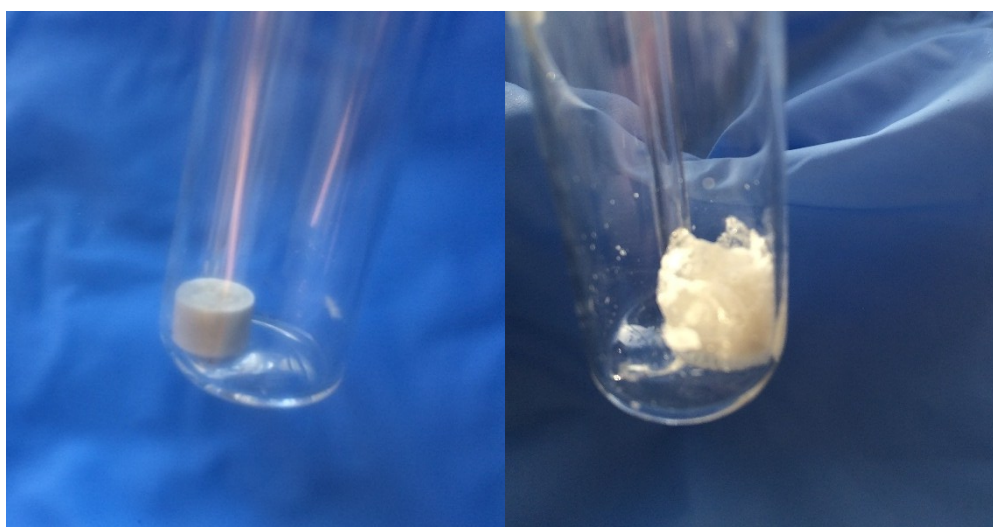


**Figure S6.** Images of a pellet of **s2** heated to 50 °C (left) and 60 °C (right) in argon atmosphere.

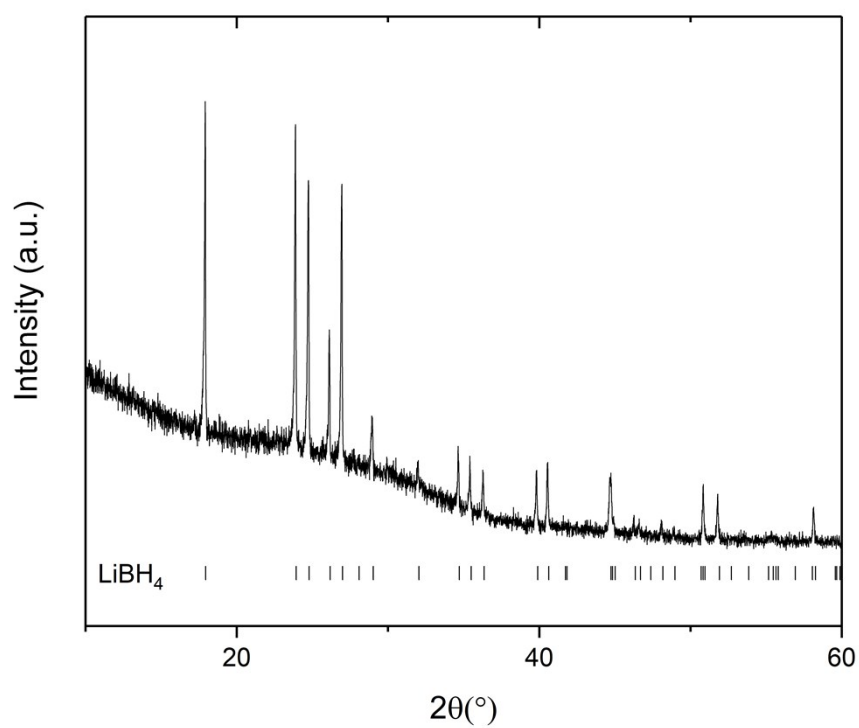


**Figure S7.** PXD pattern of **s2** after desorption at 60 °C under vacuum.

---

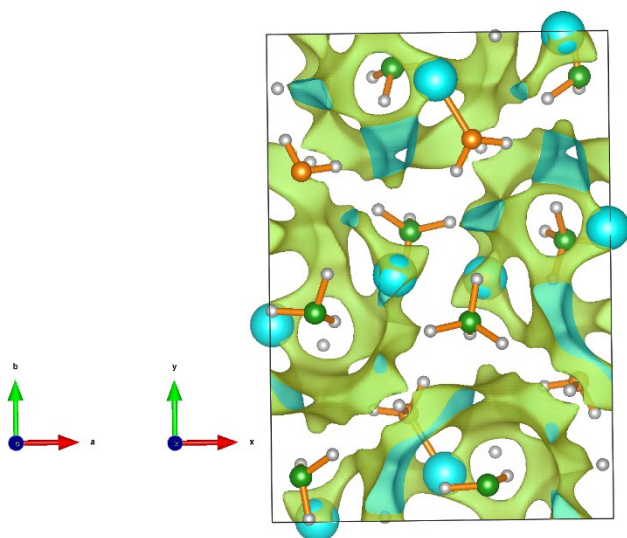


**Figure S8.** Conduction pathway for  $\text{Li}^+$  in  $\text{LiBH}_4 \cdot \frac{1}{2}\text{NH}_3$  calculated by the program SoftBV and drawn by Vesta. Li atom is shown in blue, and B is in green, N is in orange and H is in grey. Ribbons represent the conduction paths within  $a$ - $c$  layers along the  $c$ -axis. The surface seen is the minimum energy surface (green and blue are 2 sides of the surface).

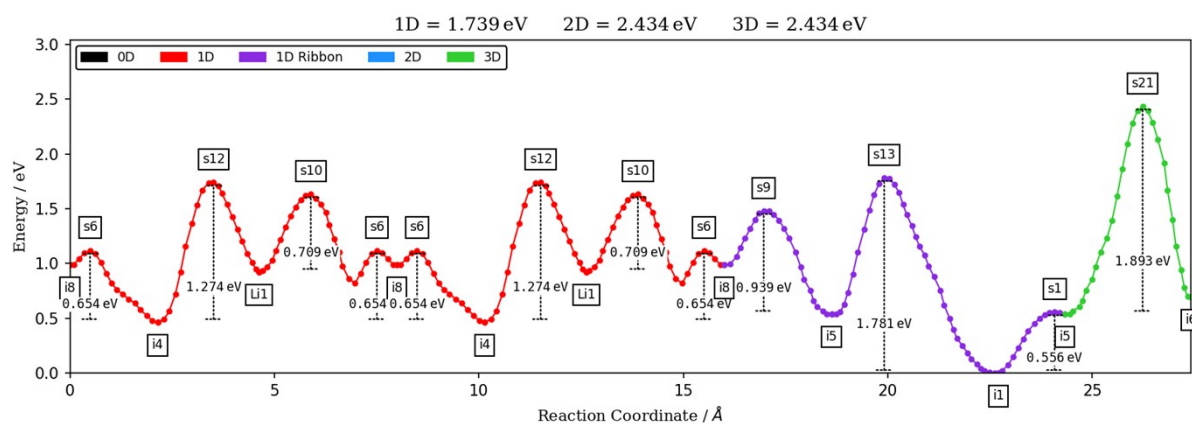


**Figure S9.** Energy barriers of  $\text{Li}^+$  ion migration pathway along the  $c$ -axis in the interlayers in the  $a$ - $c$  plane of the  $\text{LiBH}_4 \cdot \frac{1}{2}\text{NH}_3$  unit cell, calculated by the program SoftBV using Bond Valence approach. The energy barriers of the 1D pathways is calculated to be  $\sim 1$  eV, which is higher than what DFT proposed (0.16 eV). As SoftBV does not take into account the dynamics of  $\text{NH}_3$ , the low energy barriers observed and calculated by DFT are due to  $\text{NH}_3$  mediation.

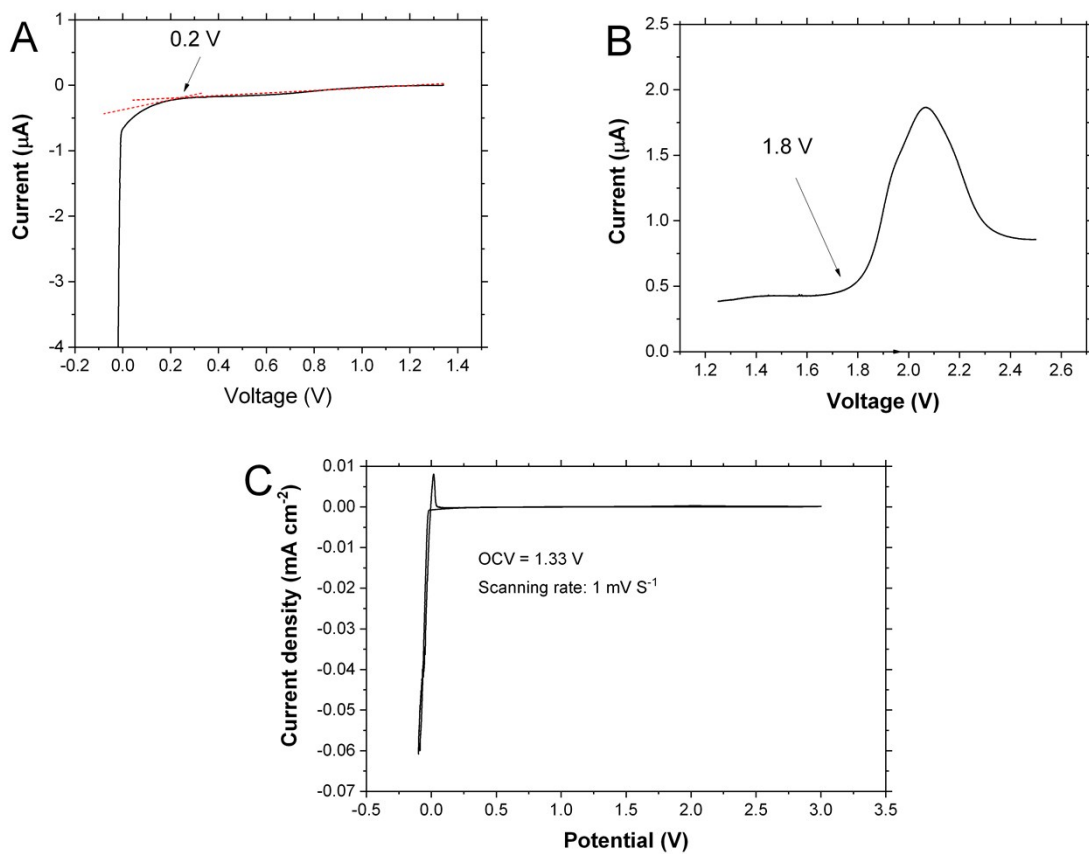


**Figure S10.** CV curves of  $\text{LiBH}_4 \cdot \frac{1}{2}\text{NH}_3$ : (A) from OCV to 0 V, (B) from OCV to 2.5V and (C) from -0.1 to 3V, using linear sweep voltammetry on a stainless-steel working electrode. Scanning rate:  $1 \text{ mV s}^{-1}$ , temperature:  $25 \text{ }^\circ\text{C}$ .

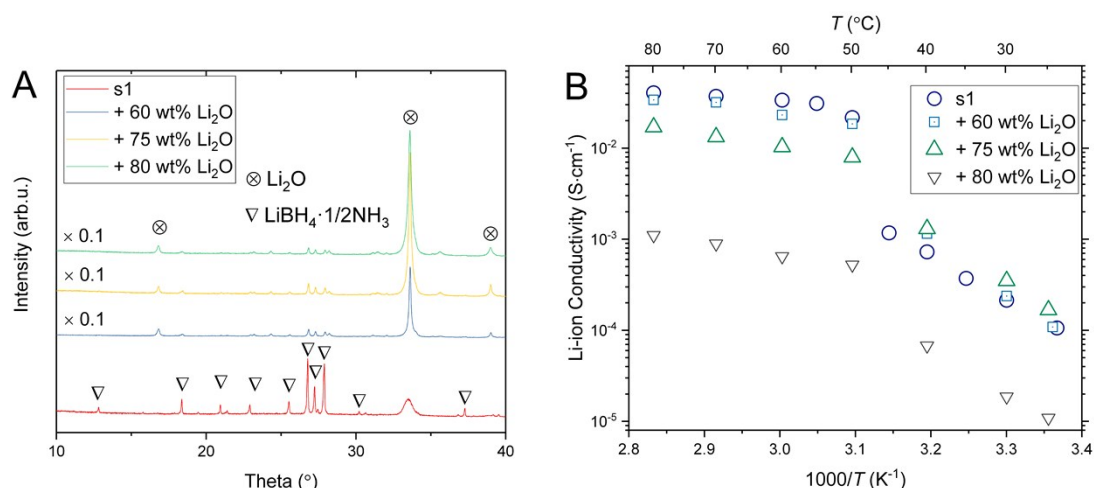


**Figure S11.** Different amounts of additional  $\text{Li}_2\text{O}$ : (A) PXD pattern and (B) Li-ion conductivity plots.

**Table S1.** Approximate compositions of  $\text{Li}_2\text{O}$  added samples

Samples	Approximate compositions
s1 + 60 wt% $\text{Li}_2\text{O}$	26.8 wt% $\text{LiBH}_4 \cdot \frac{1}{2}\text{NH}_3$ + 73.2 wt% $\text{Li}_2\text{O}$
s1 + 75 wt% $\text{Li}_2\text{O}$	16.7 wt% $\text{LiBH}_4 \cdot \frac{1}{2}\text{NH}_3$ + 83.3 wt% $\text{Li}_2\text{O}$
s1 + 80 wt% $\text{Li}_2\text{O}$	13.4 wt% $\text{LiBH}_4 \cdot \frac{1}{2}\text{NH}_3$ + 86.6 wt% $\text{Li}_2\text{O}$

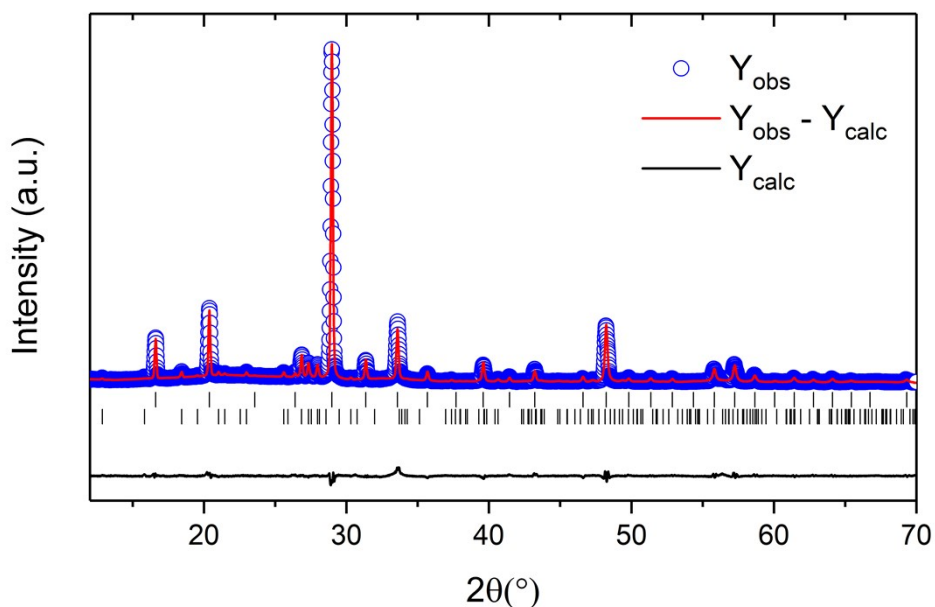


**Figure S12.** Rietveld refinement of PXD data of the  $\text{Li}(\text{BH}_4)_{0.33}(\text{NH}_2)_{0.67}$  sample reported in Ref. [14] in the manuscript,  $\lambda = 1.54056 \text{ \AA}$ , showing experimental (blue circles) and calculated (red line) PXD patterns, and a difference plot below (black line). Top tick ( $\text{LiBH}_4 \cdot \frac{1}{2}\text{NH}_3$ , 15.0 wt%), bottom tick ( $\text{Li}(\text{BH}_4)_{0.25}(\text{NH}_2)_{0.75}$ , 85.0 wt%). Final discrepancy factors:  $R_p = 5.09\%$ ,  $R_{wp} = 6.98\%$  (not corrected for background),  $R_p = 14.9\%$ ,  $R_{wp} = 14.2\%$  (conventional Rietveld  $R$ -factors),  $R_{\text{Bragg}}(\text{LiBH}_4 \cdot \frac{1}{2}\text{NH}_3) = 5.95\%$ ,  $R_{\text{Bragg}}(\text{Li}(\text{BH}_4)_{0.25}(\text{NH}_2)_{0.75}) = 11.6\%$  and global  $\chi^2 = 7.61$ .  $\text{LiBH}_4 \cdot \frac{1}{2}\text{NH}_3$ : space group  $Pna2_1$ ,  $a = 9.615(1)$ ,  $b = 13.747(2)$ ,  $c = 4.4358(5) \text{ \AA}$ ;  $\text{Li}(\text{BH}_4)_{0.25}(\text{NH}_2)_{0.75}$ : space group  $I2_13$ ,  $a = 10.6646(3) \text{ \AA}$ .

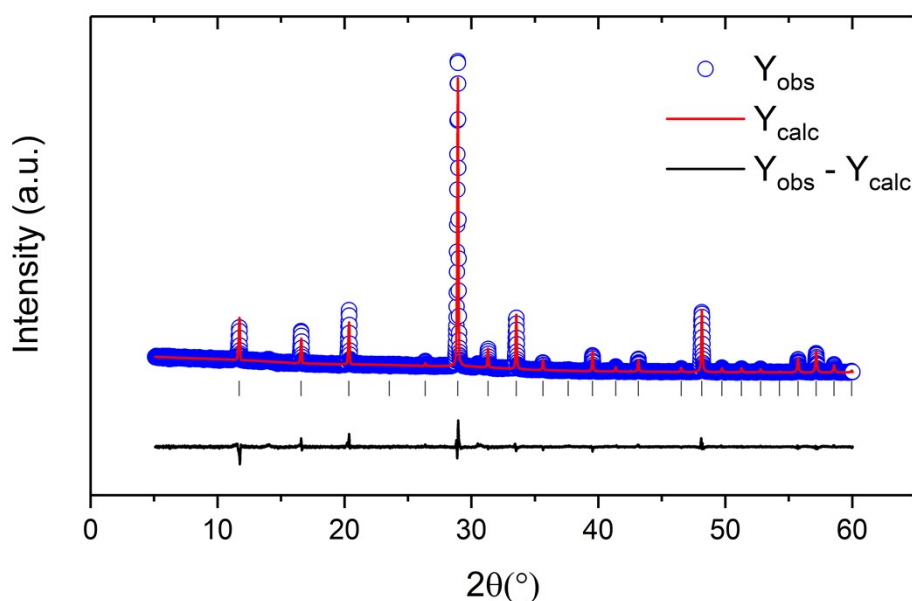


**Figure S13.** Rietveld refinement of PXD data of the  $\text{Li}(\text{BH}_4)_{0.25}(\text{NH}_2)_{0.75}$ ,  $\lambda = 1.54056 \text{ \AA}$ , showing experimental (blue circles) and calculated (red line) PXD patterns, and a difference plot below (black line). Tick:  $\text{Li}(\text{BH}_4)_{0.25}(\text{NH}_2)_{0.75}$ . Final discrepancy factors:  $R_p = 5.68\%$ ,  $R_{wp} = 7.92\%$  (not corrected for background),  $R_p = 28.2\%$ ,  $R_{wp} = 20.6\%$  (conventional Rietveld  $R$ -factors),  $R_{\text{Bragg}}(\text{Li}(\text{BH}_4)_{0.25}(\text{NH}_2)_{0.75}) = 6.37\%$  and global  $\chi^2 = 15$ .  $\text{Li}(\text{BH}_4)_{0.25}(\text{NH}_2)_{0.75}$ : space group  $I2_13$ ,  $a = 10.6804(3) \text{ \AA}$ .

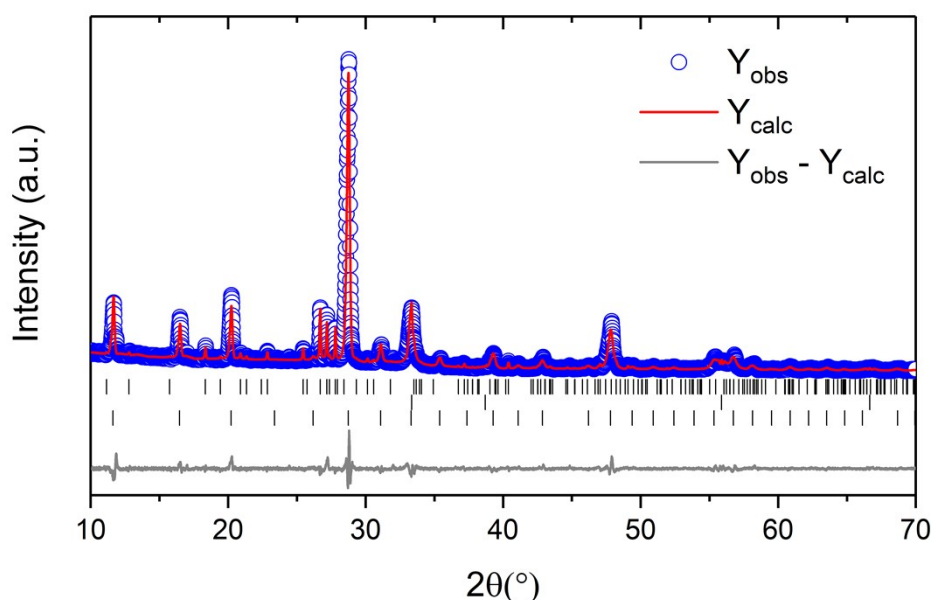
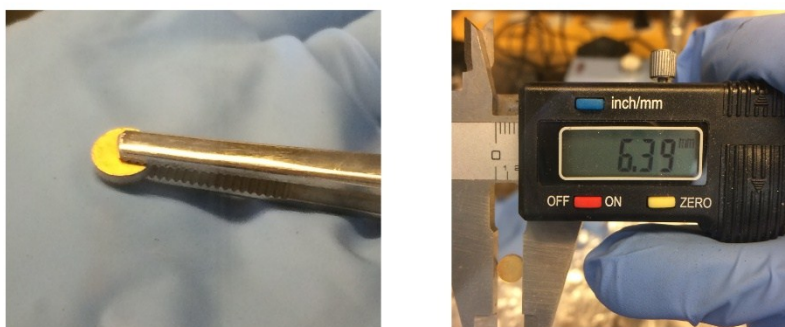


**Figure S14.** Rietveld refinement of PXD data of the sample **s3**,  $\lambda = 1.54056 \text{ \AA}$ , showing experimental (blue circles) and calculated (red line) PXD patterns, and a difference plot below (black line). Top tick ( $\text{LiBH}_4 \cdot \frac{1}{2}\text{NH}_3$ , 15.1 wt%), middle tick ( $\text{Li}_2\text{O}$ , 8.1 wt%), bottom tick ( $\text{Li}(\text{BH}_4)_{0.25}(\text{NH}_2)_{0.75}$ , 76.8 wt%). Final discrepancy factors:  $R_p = 5.9\%$ ,  $R_{wp} = 7.8\%$  (not corrected for background),  $R_p = 18.7\%$ ,  $R_{wp} = 17.4\%$  (conventional Rietveld  $R$ -factors),  $R_{\text{Bragg}}(\text{LiBH}_4 \cdot \frac{1}{2}\text{NH}_3) = 12.7\%$ ,  $R_{\text{Bragg}}(\text{Li}_2\text{O}) = 3.94\%$ ,  $R_{\text{Bragg}}(\text{Li}(\text{BH}_4)_{0.25}(\text{NH}_2)_{0.75}) = 3.79\%$  and global  $\chi^2 = 15.1$ .  $\text{LiBH}_4 \cdot \frac{1}{2}\text{NH}_3$ : space group  $Pna2_1$ ,  $a = 9.665(1)$ ,  $b = 13.829(1)$ ,  $c = 4.4627(4) \text{ \AA}$ ;  $\text{Li}_2\text{O}$ : space group  $Fm-3m$ ,  $a = 4.64924(33) \text{ \AA}$ ;  $\text{Li}(\text{BH}_4)_{0.25}(\text{NH}_2)_{0.75}$ : space group  $I2_13$ ,  $a = 10.6804(3) \text{ \AA}$ .

Before EIS measurement



Before EIS measurement

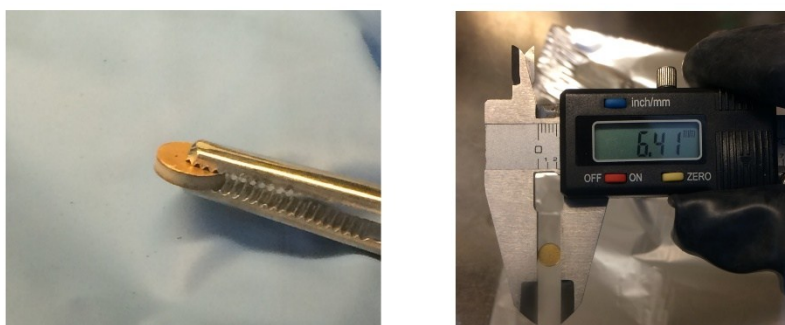


**Figure S15.** Images of a pellet of sample **s3** before and after EIS measurements, showing no shape deformation after being measured in the temperature from RT to 90 °C.

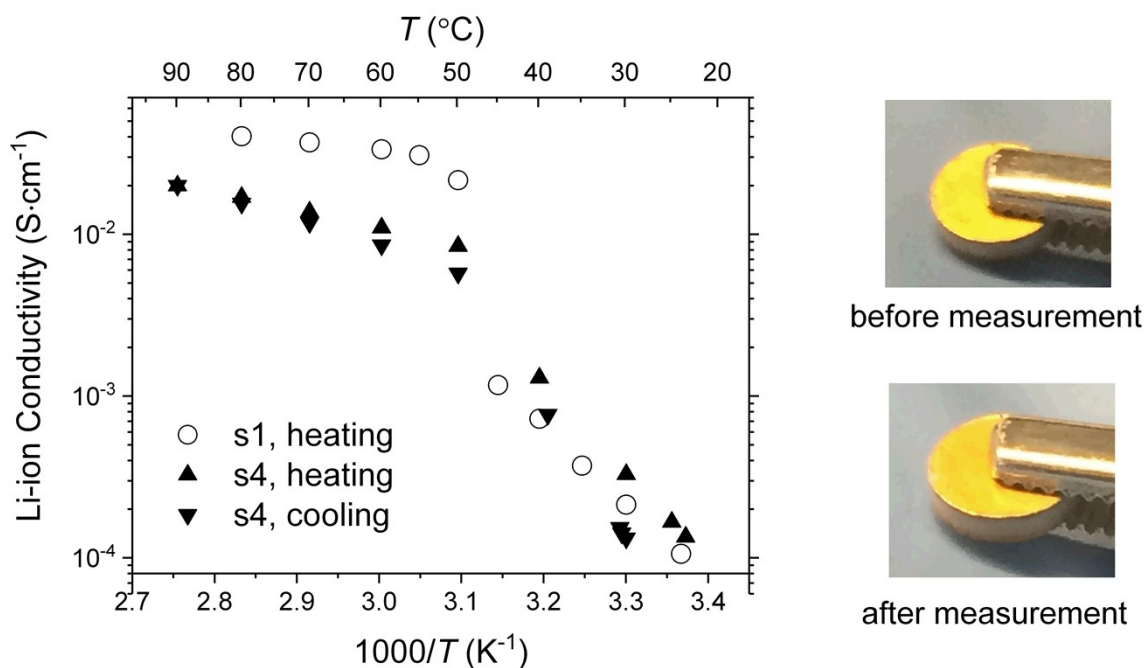


**Figure S16.** Temperature-dependent Li-ion conductivities of sample **s4**, compared to **s1** and the pellet images of sample **s4** before and after EIS measurement. No visible shape deformation of **s4** was observed after EIS measurement up to 90 °C, indicating the successful mechanical stabilization of **s1** after being mixed with Li<sub>2</sub>O powders.

**Table S2.** Activation energies extracted from the conductivity data based on the relation:

$$\ln(\sigma T) = \ln(A) - E_a/(k_b T).$$

Sample	Activation energy (LT region) (eV)	Activation energy (HT region) (eV)
s1	0.970	0.134
s4 (heating)	1.12	0.248
s4 (cooling)	1.62	0.324
s1 + 60 wt% Li <sub>2</sub> O	1.25	0.240
s1 + 75 wt% Li <sub>2</sub> O	1.12	0.290
s1 + 80 wt% Li <sub>2</sub> O	1.01	0.273

### Thermodynamic consideration of formation of LiBH<sub>4</sub>·½NH<sub>3</sub>

Reaction scheme eq. 1, may be considered as consisting of two reaction steps:



We do not have thermodynamic data of LiNH<sub>2</sub> and LiBH<sub>4</sub>·½NH<sub>3</sub>, and cannot do a quantitative thermodynamic calculation, however, qualitatively we do not expect any significant change in entropy, as no gas is released. Thus, the reaction is likely driven by the reaction enthalpy. This is supported by the very exothermic reaction between most metal borohydrides and ammonia, e.g. observed for the reaction between NH<sub>3</sub> and LiBH<sub>4</sub>, Mg(BH<sub>4</sub>)<sub>2</sub>, Ca(BH<sub>4</sub>)<sub>2</sub>, Y(BH<sub>4</sub>)<sub>3</sub>, etc.

### Supplementary references

1. G. Kresse and J. Furthmüller, *Phys. Rev. B*, 1996, **54**, 11169-11186.
2. G. Kresse and J. Furthmüller, *Comp. Mater. Sci.* 1996, **6**, 15-50.
3. J. P. a. B. Perdew, Kieron and Ernzerhof, Matthias, *Phys. Rev. Lett.* 1996, **77**, 4.
4. P. E. Blochl, *Phys. Rev. B*, 1994, **50**, 17953-17979.
5. Y.-S. Lee and Y. W. Cho, *J. Phys. Chem. C*, 2017, **121**, 17773-17779.
6. T. Ikeshoji, E. Tsuchida, T. Morishita, K. Ikeda, M. Matsuo, Y. Kawazoe and S.-i. Orimo, *Phys. Rev. B*, 2011, **83**, 144301.
7. J. Cuan, Y. Zhou, T. Zhou, S. Ling, K. Rui, Z. Guo, H. Liu and X. Yu, *Adv. Mater.* 2019, **31**, 1803533.
8. G. Henkelman, B. P. Uberuaga and H. Jonsson, *J. Chem. Phys.* 2000, **113**, 9901-9904.
9. H. Chen, L. L. Wong and S. Adams, *Acta. Cryst. B*, 2019, **75**, 18-33.
10. K. Momma and F. Izumi, *J. Appl. Crystallogr.* 2011, **44**, 1272-1276.
11. S. R. Johnson, W. I. F. David, D. M. Royse, M. Sommariva, C. Y. Tang, F. P. A. Fabbiani, M. O. Jones and P. P. Edwards, *Chem. Asian. J.* 2009, **4**, 849-854.